# Long Baseline Observations of the HD 100546 Protoplanetary Disk with ALMA

Sebastián Pérez[1,2] , Simon Casassus[2] , Antonio Hales[3,4] , Sebastián Marino[5] , Anthony Cheetham[5,6] , Alice Zurlo[7,8] ,
Lucas Cieza[7] , Ruobing Dong[9] , Felipe Alarcón[10] , Pablo Benítez-Llambay[11] , Ed Fomalont[3,4] , and Henning Avenhaus[5]

[1] Universidad de Santiago de Chile, Av. Libertador Bernardo O'Higgins 3363, Estación Central, Santiago, Chile; sebastian.astrophysics@gmail.com
[2] Departamento de Astronomía, Universidad de Chile, Casilla 36-D, Santiago, Chile
[3] National Radio Astronomy Observatory, 520 Edgemont Road, Charlottesville, VA 22903-2475, USA
[4] Atacama Large Millimeter/Submillimeter Array, Joint ALMA Observatory, Alonso de Córdova 3107, Vitacura 763-0355, Santiago, Chile
[5] Max Planck Institute for Astronomy (MPIA), Königstuhl 17, D-69117 Heidelberg, Germany
[6] Observatoire de Genève, Université de Genève, 51 chemin des Maillettes, 1290 Versoix, Switzerland
[7] Universidad Diego Portales, Av. Ejercito 441, Santiago, Chile
[8] Escuela de Ingeniería Industrial, Facultad de Ingeniería y Ciencias, Universidad Diego Portales, Av. Ejercito 441, Santiago, Chile
[9] Department of Physics & Astronomy, University of Victoria, Victoria, BC, V8P 1A1, Canada
[10] Department of Astronomy, University of Michigan, 1085 S. University, Ann Arbor, MI 48109, USA
[11] Niels Bohr International Academy, Niels Bohr Institute, Blegdamsvej 17, DK-2100 Copenhagen Ø, Denmark

## Abstract

Using the Atacama Large Millimeter/submillimeter Array, we observed the young Herbig star HD 100546, host to a prominent disk with a deep, wide gap in the dust. The high-resolution 1.3 mm continuum observation reveals fine radial and azimuthal substructures in the form of a complex maze of ridges and trenches sculpting a dust ring. The $^{12}$CO(2–1) channel maps are modulated by wiggles or kinks that deviate from Keplerian kinematics particularly over the continuum ring, where deviations span 90° in azimuth, covering ∼5 km s$^{-1}$. The most pronounced wiggle resembles the imprint of an embedded massive planet of at least 5 $M_{Jup}$ predicted from previous hydrodynamical simulations. Such a planet is expected to open a deep gap in both gas and dust density fields within a few orbital timescales, yet the kinematic wiggles lie near ridges in the continuum. The lesser strength of the wiggles in the $^{13}$CO and C$^{18}$O isotopologues show that the kinematic signature weakens at lower disk heights, and suggests qualitatively that it is due to vertical flows in the disk surface. Within the gap, the velocity field transitions from Keplerian to strongly non-Keplerian via a twist in position angle, suggesting the presence of another perturber and/or an inner warp. We also present Very Large Telescope/SPHERE sparse aperture masking data that recover scattered light emission from the gap's edges but show no evidence for signal within the gap, discarding a stellar binary origin for its opening.

## 1. Introduction

Substructures in protoplanetary disks are not only ubiquitous but also diverse. Radial gaps, fine and wide rings, spiral arms, and lopsided concentrations are among the most common substructures found in resolved observations of disks. The mechanisms behind the formation of such varied structures are not entirely known, but most models invoke planet–disk interactions. It appears that these substructures are a common feature of the early evolution of protoplanetary disks and it is widely thought that they are related to the process of planet formation.

Radial discontinuities and concentric rings appear to be the most frequent substructures, such as in HL Tau (ALMA Partnership et al. 2015), TW Hya (Andrews et al. 2016), HD 97048 (van der Plas et al. 2017), HD 169142 (Fedele et al. 2017; Pérez et al. 2019a), and the disks in the Disk Substructures at High Angular Resolution Project (Andrews et al. 2018). These dusty annuli can be sculpted by planets (e.g., Dipierro et al. 2015) that usually leave a clear gap in the dust radial profile. In the case of a low-mass planet, the planet–disk interaction can produce multiple narrow gaps and rings (e.g., Dong et al. 2017). For example, Pérez et al. (2019a) showed that a migrating mini-Neptune planet can reproduce the three fine rings observed in the HD 169142 transition disk (see also Weber et al. 2019).

Simulations of planet–disk interactions show that young massive planets develop a circumplanetary disk (CPD) as they accrete material from their parent protoplanetary disk (e.g., Miki 1982; Lubow et al. 1999; Gressel et al. 2013; Szulágyi et al. 2014). The CPDs persist for as long as the planet grows. CPDs, however, are difficult to detect in dust continuum (Ricci et al. 2017; Wu et al. 2017; Pérez et al. 2019b). The protoplanet candidates inside the gap of PDS 70 are the only detections that have not been challenged so far (Keppler et al. 2018; Christiaens et al. 2019). Recently, submillimeter emission attributed to dust emission from a CPD around PDS 70c has been reported, as well as dust orbiting in proximity of PDS 70b (Isella et al. 2019). Indeed, the radio flux emitted by these CPDs may be very faint because millimeter dust is believed to be lost by radial drift within a few hundred years (Zhu et al. 2018).

In Perez et al. (2015), we show that a giant planet embedded in a circumstellar disk produces distinct kinematical signatures, detectable in CO velocity maps when probed at high resolution and sensitivity. One of the predicted characteristics of a massive planet is a wiggle or kink in the isovelocity contours of CO emission in the vicinity of the planet. The terms twist (Perez et al. 2015), kink (Pinte et al. 2018), and wiggle (Pérez et al. 2018) have all been used to refer to a kinematic deviation associated with an embedded planet. In this work, we opt for the word wiggle. Pinte et al. (2018) observed such a wiggle in

isovelocity maps of HD 163296, identifying the presence of a giant planet at 260 au. Teague et al. (2018), using azimuthally averaged kinematic information, measured the pressure profile of a gap that is consistent with a planet opening mechanism. Recently, Pinte et al. (2019) also found a wiggle coincident with the gap in the continuum map of HD 97048.

In this Letter, we present 1.3 mm observations of HD 100546 at $\lesssim 2$ au resolution in continuum and $\lesssim 8$ au resolution in the CO(2–1) isotopologues molecular lines (Section 2). We describe the substructures observed in the continuum in Section 3.1. The $^{12}$CO gas moment maps are described in Section 3.2. A kinematic wiggle coincident with the continuum ring is presented in Section 3.2.1. The deviations from the azimuthally symmetric flow are quantified and discussed in a companion Letter (Casassus & Pérez 2019). The velocity perturbations where the wiggle is more pronounced show similarities with those expected for an accreting giant. New infrared observations, presented in Section 3.3, rule out the presence of stellar companions inside the dust gap. A discussion of the nature of the kinematic detection and the puzzling association with the bright continuum ring is presented in Section 4. Throughout this Letter, we assume a distance of $110.0 \pm 0.6$ pc to HD 100546 (Gaia Collaboration et al. 2018).

## 2. Observations

### 2.1. ALMA Continuum and Molecular Line Observations

We obtained 1.3 millimeter observations of HD 100546 with the Atacama Large Millimeter/submillimeter Array (ALMA) by combining the 12 m array in extended (C40–9) and compact (C40–6) configurations, in the context of Cycle 4 project 2016.1.00344.S. The resulting baselines ranged from 19 m to up to 12.2 km with a total of 39–42 antennas. The combined observations are sensitive to spatial scales of up to 1″.5. The long baseline observations were acquired on 2017 September 19, 22, and 23, in three different blocks of ~90 minutes each (40 minutes on source). Precipitable water vapor ranged between 0.3 and 0.8 mm. Observations of atmospheric (J1147–6753), bandpass (J0635–7516), and flux (J1107–4449) calibrators were performed. The phase calibrator (J1147–6753) was alternated with the science target to calibrate the time-dependent variation of the complex gains. The cycling time for phase calibration was set to 8 minutes and 54 s for the compact and extended configurations, respectively. The ALMA correlator was configured in Frequency Division Mode. Two spectral windows with 1.875 GHz bandwidth were set up for detecting the dust continuum, centered at 232.005 GHz, and 218.505 GHz, respectively. The $^{12}$CO(2–1), $^{13}$CO(2–1), and C$^{18}$O(2–1) transitions of carbon monoxide were targeted by configuring three spectral windows at rest frequencies of 230.538 GHz, 220.399 GHz and 219.560 GHz respectively. The spectral resolution for the line observations was 122.070 kHz (equivalent to 0.2 km s$^{-1}$ channels).

All data were calibrated by the ALMA staff using the ALMA Pipeline version 40896 in the CASA package (McMullin et al. 2007), including offline Water Vapor Radiometer calibration, system temperature correction, as well as bandpass, phase, and amplitude calibrations. The short baseline and long baseline data sets were calibrated independently.

Synthesis imaging was initially carried out using the CLEAN algorithm (CASA version 5.4, task `tclean`). Self-calibration of the data was performed to improve coherence. A signal-to-noise

ratio (S/N) of ~80 was achieved prior to self-calibration. One round of phase self-calibration using a solution interval of 54 s was applied to the data, which was found to improve the resulting S/N by a factor of 1.6. A positional offset between short and long baseline was corrected prior to combining the data sets. An image reconstructed using natural weights, after self-calibration and concatenation of the data sets, yields an rms noise of 12 $\mu$Jy beam$^{-1}$, for a CLEAN beam of $64 \times 45$ mas.

As HD 100546 is bright in the millimeter, we super-resolved the self-calibrated continuum data using nonparametric image modeling with the `uvmem` package (here we used the publicly available GPU adaptation `gpuvmem`[12]; Cárcamo et al. 2018). Image positivity provided enough regularization (i.e., we did not add entropy to the objective function). The `uvmem` reconstruction $I_{1.3\,mm}$ provides slightly higher angular resolutions than super-uniform weighting, but without compromising sensitivity (see Cárcamo et al. 2018 for details). We adopted the `uvmem` image for our analysis.

The effective angular resolution of the `uvmem` model was measured with an elliptical Gaussian fit to a deconvolution of a simulation with the same $uv$-coverage as the ALMA observation taken on a single spike. The input spike flux was 10 mJy, which is comparable with the emission at the location of the central star. The final $I_{1.3\,mm}$ image has an angular resolution of $\Omega_b = 19.7 \times 12.9$ mas, or $2.1 \times 1.4$ au. This effective beam is consistent with the expectation of $\lesssim 1/3$ the natural beams (Cárcamo et al. 2018), which is $\Omega_{nat} = 64 \times 45$ mas. We oversampled $\Omega_b$ with 2.5 mas pixels. The peak in flux is 0.92 mJy beam$^{-1}$, at the location of the star. The flux density of the central source is $3.1 \pm 0.3$ mJy, while the total flux density over the entire image is $436 \pm 40$ mJy.

We estimate that the noise level in the $I_{1.3\,mm}$ image is 16.6 $\mu$Jy beam$^{-1}$, where beam = $19.7 \times 12.9$ mas. The following conservative approach was used to obtain this estimate. We first measured the noise in the restored image (comparable to a CLEAN restoration), in natural weights. This was done by calculating the standard deviation inside small boxes devoid of bright continuum emission, but including synthesis imaging artifacts. This measurement was repeated over several regions, and the largest standard deviation was adopted as systematic noise. This amounts to $\sigma_{total} = 56$ $\mu$Jy beam$^{-1}$, in the $\Omega_{nat}$ beam. Second, we assumed that the noise in $I_{1.3\,mm}$ was worse by a factor of $\sqrt{N_b}$, where $N_b \sim 11.4 = \Omega_{nat}/\Omega_b$ is the number of `uvmem` beams inside the natural-weight beams. The resulting noise level in $I_{1.3\,mm}$ is thus $\sigma_{MEM} = 16.6$ $\mu$Jy beam$^{-1}$, in the $\Omega_b$ `uvmem` beam, after dividing for $\Omega_{nat}/\Omega_b$. A similar estimate of the noise level can be obtained by assuming that a perfect deconvolution would yield the same point-source sensitivity as the dirty map in natural weights, with the thermal noise in natural weights.

Channel maps of CO(2–1) emission were constructed with `tclean`. We used a Briggs weighting scheme with a robust parameter of 1.0 for $^{12}$CO, which yields the best results in terms of achieving good signal to noise without compromising on resolution. Channel maps were produced with a spectral resolution of 0.5 km s$^{-1}$. Each channel map has an rms noise of 1.3 mJy beam$^{-1}$, for a CLEAN beam of $76 \times 57$ mas. Line emission cubes were produced with and without prior continuum subtraction (performed with CASA task `uvcontsub`). For the
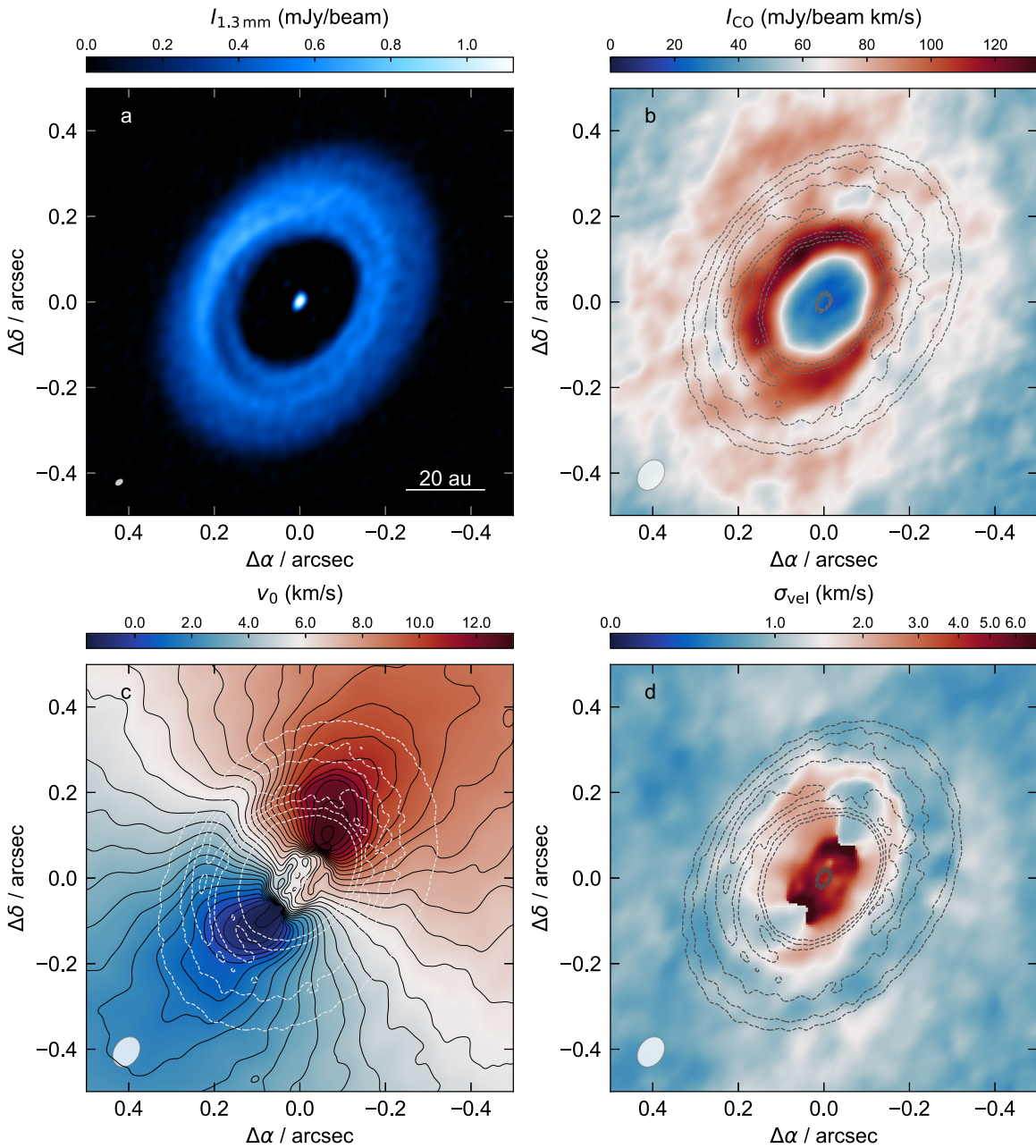
---

[12] https://github.com/miguelcarcamov/gpuvmem

**Figure 1.** ALMA observations of HD 100546 acquired in 2017 September. (a) Dust continuum emission map at 1.3 mm ($I_{1.3 \, \mathrm{mm}}$). (b) $^{12}$CO intensity map (zeroth moment, $I_{\mathrm{CO}}$). (c) Velocity map (first moment, $v_0$) from $^{12}$CO(2–1) emission that shows perturbed non-Keplerian flows at the location of the continuum ring. (d) $^{12}$CO velocity dispersion map (second moment, $\sigma_{\mathrm{vel}}$). Contours of $I_{1.3 \, \mathrm{mm}}$ are plotted over moment maps with levels 0.15, 0.27, 0.40, 0.52, and 0.64 mJy beam$^{-1}$. The lowest contour corresponds to $9\sigma_{\mathrm{MEM}}$. All panels display the same field of view.

$^{13}$CO and C$^{18}$O isotopologues, a Briggs robust parameter of 2.0 was used given the low signal in those lines, yielding maps with a beam resolution of 82 × 61 mas and rms noise of 1.8 and 1.2 mJy beam$^{-1}$, respectively. Here, we present the CO maps with continuum subtraction ($^{12}$CO maps without prior continuum subtraction can be found in Casassus & Pérez 2019). The $^{12}$CO moment zero was calculated using an intensity-weighted sum along the spectral axis, while first and second moments were determined via Gaussian fits to the velocity profile along each pixel. In the case of the cubes without prior continuum subtraction, the continuum emission is accounted for by a polynomial baseline when producing moment maps from Gaussian fits. The Gaussian fits work best at recovering the broad and velocity-structured

emission profiles within the gap. The rms noise in the moment zero map is ∼3 mJy beam$^{-1}$ km s$^{-1}$. We checked that channelization effects (e.g., Christiaens et al. 2014) are not present in the moment maps by producing a cube with smaller channels (0.25 km s$^{-1}$) shifted by 0.1 km s$^{-1}$ in velocity. The low signal in $^{13}$CO and C$^{18}$O prevents the recovery of good quality moment maps.

## 2.2. SPHERE Sparse Aperture Masking

To assess whether there are any stellar companions within the gap, we performed sparse aperture masking (SAM) observations with the Spectro-Polarimetric High-contrast Exoplanet REsearch
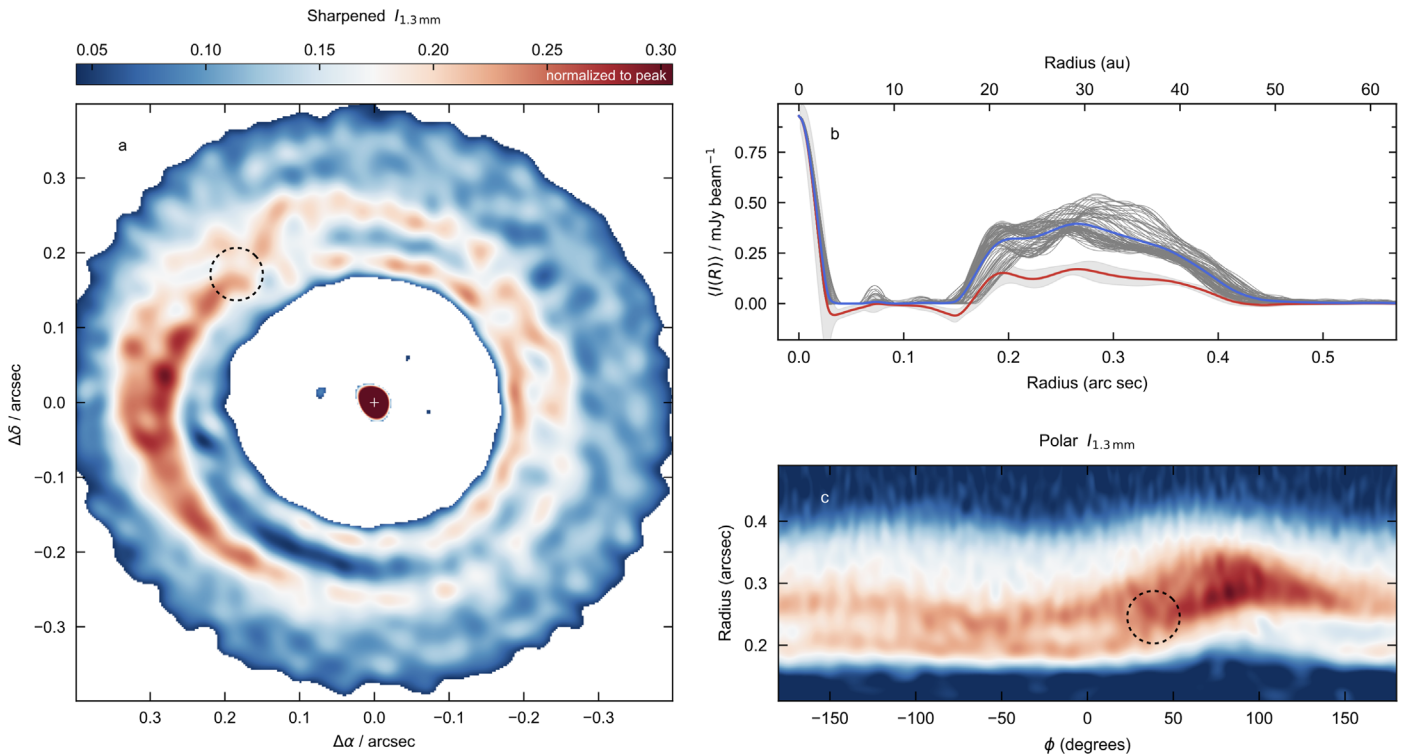
**Figure 2.** (a) Sharpened version of the 1.3 mm continuum map $I_{1.3\,mm}$ shown in Figure 1(a), using an unsharp-masking procedure to enhance the fine structure of the continuum ring. The image is deprojected to show a face-on view. (b) Surface brightness profiles from the original $I_{1.3\,mm}$ image. The blue solid line corresponds to the azimuthally averaged radial profile, while the family of thin gray curves correspond to profiles extracted from 3°.6 wedges covering the full azimuthal range. The solid red curve shows the azimuthally averaged profile of the sharpened imaged shown in panel (a). The shaded area around the profile corresponds to the dispersion around the mean. (c) Polar deprojection of $I_{1.3\,mm}$, zoomed on the continuum ring. The circle in (a) and (c) shows the approximate location of the Doppler flip seen in $^{12}$CO gas.

(SPHERE) InfraRed Dual-band Imager and Spectrograph (IRDIS) and Integral Field Spectrograph (IFS) instruments on the Very Large Telescope (VLT). The observations were acquired in 2018 May 15–16, in the K1K2 band, with 1 hr integration on HD 100546 plus 1 hr on calibrators. The data processing follows the same procedure as in Cheetham et al. (2019). The data were cleaned using the SPHERE Data Reduction and Handling pipeline (Pavlov et al. 2008), including background subtraction, flat-fielding, and extraction of the spectral data cube. IRDIS and IFS images are produced using the MIRA package (Thiébaut 2008) applied to the closure phases and visibilities, with a hyperbolic regularization term. The weights in the regularization were varied in order to suppress speckles.

## 3. Results

### 3.1. A Structured Continuum Ring

The ALMA observations of HD 100546 are summarized in Figure 1. The first panel (a) shows a bright ring in continuum emission (the ring has previously been imaged, most recently by Pineda et al. 2019, in 0.88 mm emission at 50 × 30 mas resolution). In these new images, at 20 × 13 mas resolution, the ring displays remarkable radial and azimuthal substructures. These substructures are further emphasized in an unsharp-masked version of the continuum image shown in Figure 2. This sharper image is obtained as the difference between the original $I_{1.3\,mm}$ map and its smoothed version, after convolution with a circular Gaussian kernel ($\sigma = 60$ mas). The procedure is equivalent to removing low spatial frequencies and enhances the small-scale features (Stolker et al. 2017). The sharpened image highlights

intriguing breaks in the arcs conforming the ring, especially at position angle (PA) = 80°, where the substructures split into two branching arms. The maze of ridges may suggest a complex dynamical scenario at play within the ring.

Figure 2 also shows the image transformed into polar coordinates and its azimuthally averaged surface brightness radial profile. The polar deprojection was carried out following the procedure outlined in Pérez et al. (2019a), adopting the disk orientation derived in Casassus & Pérez (2019). The offset between the center of the ring and the stellar position reveals that the ring is eccentric (as quantified in Pineda et al. 2019).

Continuum emission is detected around the location of the star. The emission is resolved with a radius of ∼1.8 au (half the FWHM along its major axis) at 19.7 × 12.9 mas resolutions. We interpret this as thermal emission from an asymmetric inner disk. However, the shape of this central emission could be affected by the point-spread function.

Several compact features are present inside the gap (see Figure 2). The brightest of these features is 5σ; however, it is most likely an image synthesis artifact due to its proximity to the sidelobe of the natural-weighted beam. Any other signals inside the gap are at ⩽3σ.

### 3.2. Gas Kinematics

#### 3.2.1. Kinematic Signature over the Continuum Ring

The long baseline ALMA observations presented here were part of a program to reach high enough sensitivities to map the velocity field of HD 100546 at fine angular scales. The
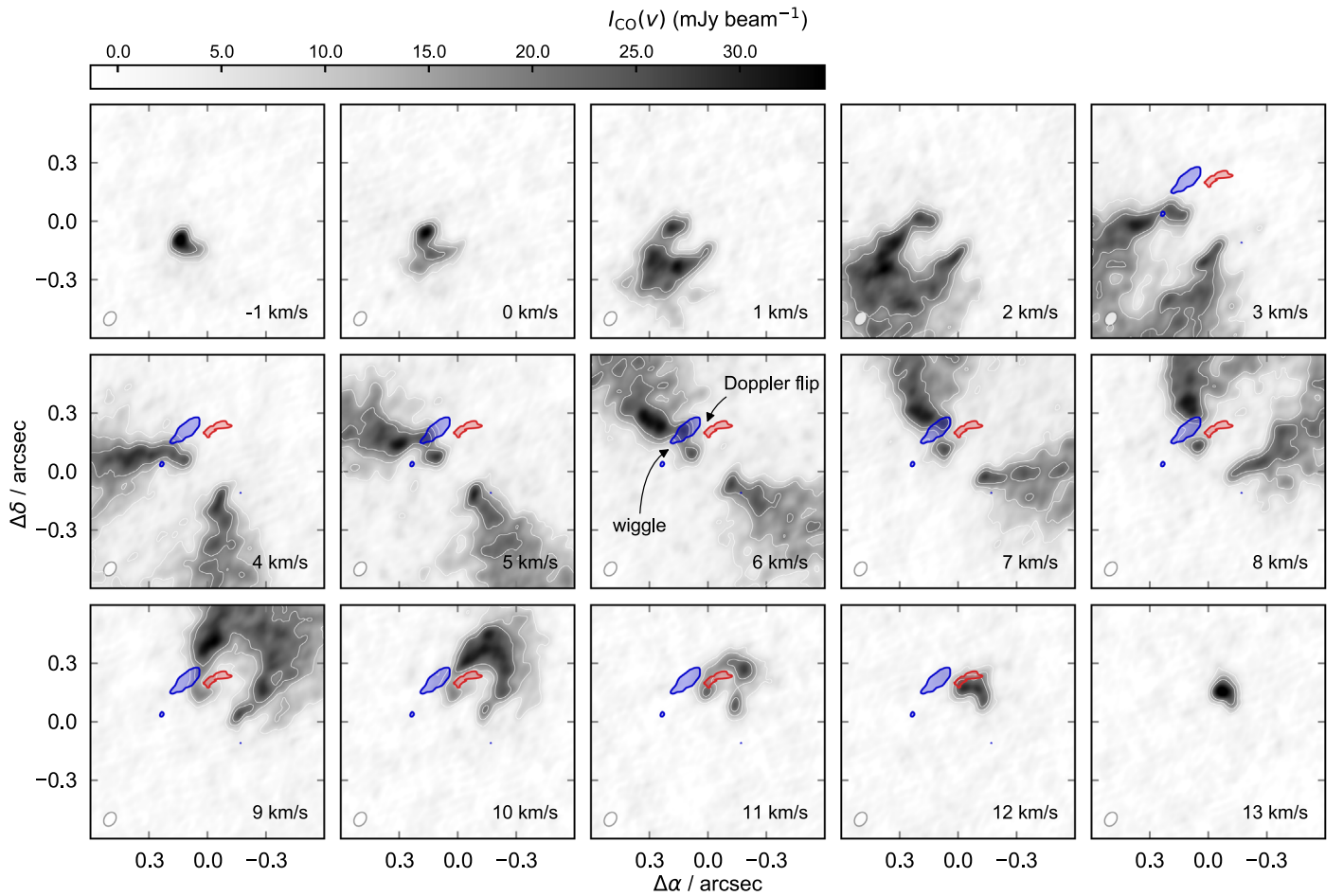
**Figure 3.** $^{12}$CO emission channel maps of HD 100546 showing several non-Keplerian structures. Most strikingly, it shows velocity "wiggles" (or kinks) between $0\rlap{.}''2$ and $0\rlap{.}''3$ separation northeast from the star. This local non-Keplerian feature can be seen in channels between $+3$ and $+8$ km s$^{-1}$ in velocity. The Doppler flip in the deviation from axially symmetric kinematics (presented in Casassus & Pérez 2019) is shown as blue and red filled contours. The wiggle and Doppler flip labeled in the panel at $+6$ km s$^{-1}$. Each panel shows $^{12}$CO emission sampled every 1 km s$^{-1}$ (although the channel width is 0.5 km s$^{-1}$). Contours correspond to 5, 10, and 15 times the channel rms (1.3 mJy beam$^{-1}$). The synthesized beam of the CLEAN reconstruction is shown in the bottom left corner.

$^{12}$CO(2–1) moment maps for intensity (zeroth moment, $I_{\rm CO}$), velocity field (first moment, $v_0$), and velocity dispersion (second moment, $\sigma_{\rm vel}$) are presented in Figure 1. Individual channel maps are presented in Figure 3.

The velocity map $v_0$ is shown in Figure 1(c). At separations comparable to the continuum ring radius, the isovelocity contours in the near side of the disk (southwest, bottom right) display a symmetric pattern with respect to the disk minor axis. Interestingly, the pattern becomes highly asymmetrical on the far side (northeast, top left), especially near the continuum peak, approximately $0\rlap{.}''24$ northeast of the central star. The location of the wiggles extend over ~90° in azimuth.

As stated earlier, significant deviations from Keplerian motion can be attributed to planet–disk interactions, via the local flow in a CPD and the planet-launched spiral wakes. However, we note that other effects can also produce such wiggles in the isovelocity contours. For example, an optically thick continuum, such as the one in HD 100546, blocks the CO emission from the back side of the disk, inducing structure in the gas velocity map. This is indeed the case for the wiggle-like morphology seen in the southwest in the first moment, where the wiggles bear a reflection symmetry with respect to the disk minor axis. If the wiggles are due to planet–disk interaction kinematics, the location of the embedded perturber can be identified via a local Doppler flip in molecular line moment 1 maps, after subtraction of the axially symmetric flow (Pérez et al. 2018), which follows the disk rotation curve. Such sign reversal in the Keplerian deviation map is indeed associated with the kinematic signature found between $0\rlap{.}''2$ and $0\rlap{.}''3$ in HD 100546 (this analysis is presented in Casassus & Pérez 2019). The magnitude of the Doppler flip as well as the morphology of the wiggles resemble that of an embedded massive planet of 5–10 $M_{\rm Jup}$ as shown in previous hydrodynamical simulations (see Pérez et al. 2018, their Figure 3).

The wiggles associated with the Doppler flip can be recognized directly in the isovelocity channel maps (Figure 3), most clearly between 5.0 and 8.0 km s$^{-1}$. These wiggles are indeed easily connected with the "blue" part of the Doppler flip signal. On the other hand, the red counterpart corresponds to a deficit of signal between 9 and 11 km s$^{-1}$, replaced by signal at 12 km s$^{-1}$. If the non-Keplerian kinematics are due to a compact body, the location of the perturber can be pinpointed via the Doppler flip. As the Doppler flip is located between ridges in the maze of substructures seen in the continuum ring (see the sharpened 1.3 mm map in Figure 2), this would mean the perturber is still embedded in the dust ring.
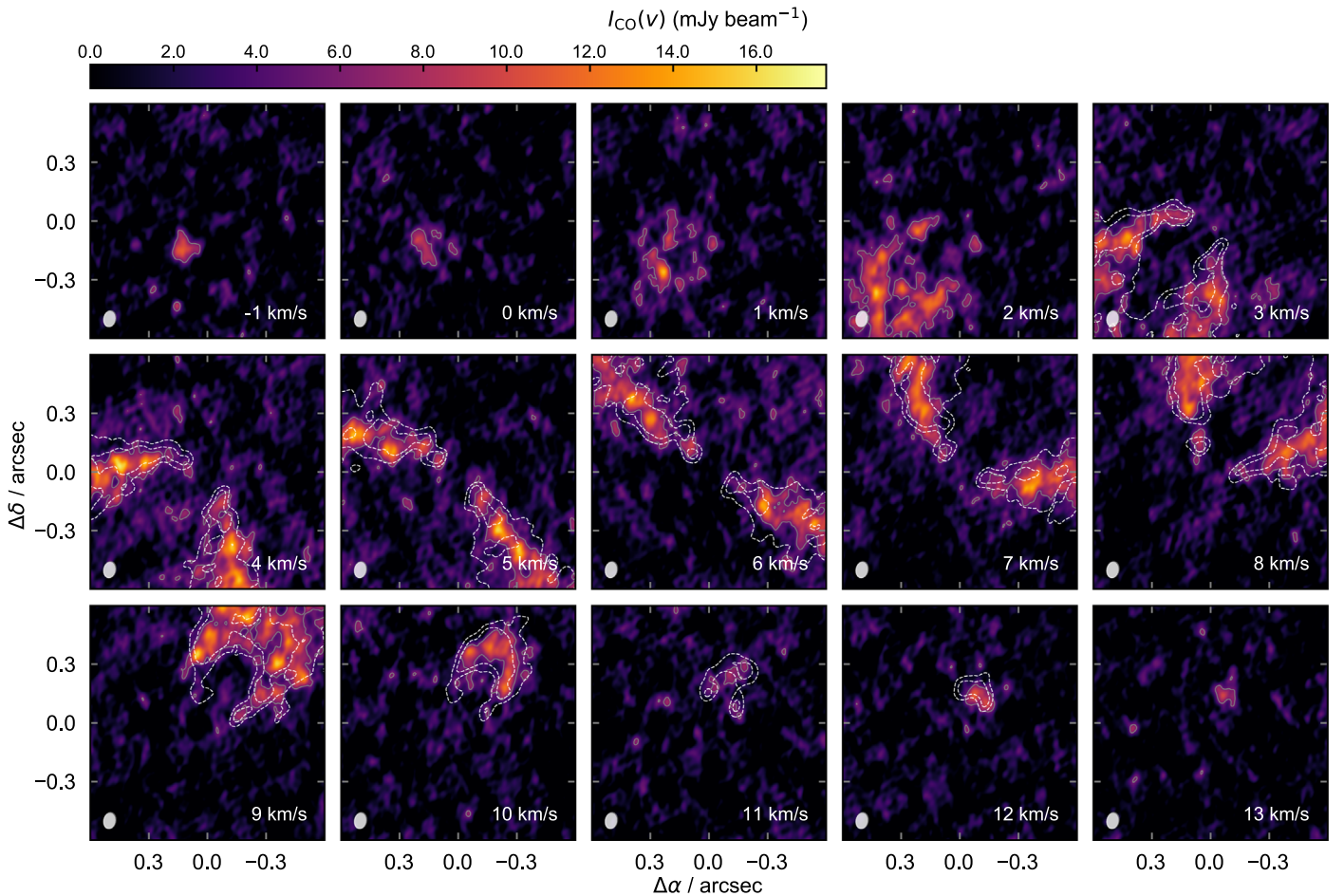
**Figure 4.** Same as Figure 3, but for $^{13}$CO emission. The white dashed contours show the corresponding $^{12}$CO emission at 10 and 16 times the $^{12}$CO maps rms, while the gray solid contour shows $^{13}$CO at 3 times the rms level. The 7 km s$^{-1}$ channel most clearly shows that $^{13}$CO do not exhibit the same obvious wiggle as in $^{12}$CO.

### 3.2.2. Vertical Structure of the Wiggle via Isotopologue Emission

Figure 4 shows that the $^{13}$CO channel maps do not exhibit any obvious wiggles, as seen in $^{12}$CO. This is most easy to notice in the 7 km s$^{-1}$ panel where the $^{13}$CO emission does not follow the morphology of the clear wiggle seen in $^{12}$CO (shown as white dashed contours). At 6 km s$^{-1}$ there is only a hint for a kinematic deviation in $^{13}$CO, while the wiggle is notorious in $^{12}$CO. The same can be said for the C$^{18}$O emission shown in Figure 5. These rarer CO isotopologues have lower optical depths and thus trace deeper layers in the disk, suggesting that the kinematic signature weakens at lower heights. Interestingly, the three isotopologues show a decrement in emission at the location where the Doppler flip transitions from blue to red.

In an idealized disk as used in hydrodynamic simulations the vertical velocities must cancel at the midplane due to mirror symmetry. On the other hand, observational arguments suggest that the bulk of the Doppler flip signal is either due to radial or vertical flows (Casassus & Pérez 2019). Thus, the qualitative absence of kinematic wiggles in the rarer isotopologues is consistent with them being mostly due to vertical motions in the disk surface.

### 3.2.3. Non-Keplerian Kinematics within the Gap

The $^{12}$CO intensity $I_{CO}$ shows an inner depletion of gas emissions within the continuum gap. Although the gap is entirely cleared in the dust, it appears filled with CO gas. Within the gap, diffuse CO emission averages 30 mJy beam$^{-1}$ km s$^{-1}$ with a scatter of 6 mJy beam$^{-1}$ km s$^{-1}$. This is not inconsistent with a planetary origin for the gap clearing as residual gas is expected to remain and be detectable in optically thick tracers such as CO (e.g., Ober et al. 2015; Facchini et al. 2018).

The gas flow within the dust gap is highly perturbed at radii <60 mas (see Figure 2(c)). Within this radius, the gas rotation pattern twists its position angle by almost 90°, more than could be explained by stellocentric accretion, even at freefall rates (e.g., Casassus et al. 2015). These deviations are manifested along all position angles, hinting at large-scale kinematic effect such as strong radial inflows and a warp, or reflecting planet–disk interaction kinematics, which can also explain deviations covering wide azimuthal ranges with an accreting giant, as shown in Pérez et al. (2018). If a perturber in an inclined orbit is present within the gap, it could drive warping of the inner regions, as in the cavity of HD 142527 (Casassus et al. 2015; Price et al. 2018). HD 142527 indeed harbors a $\sim$0.2$M_\odot$ star that has been detected with SAM observations (Biller et al. 2014) and H$\alpha$ high-contrast imaging (Close et al. 2014).

Several companion candidates have been reported in HD 100546. Quanz et al. (2013) present candidate "b" at 0."5, while Currie et al. (2015) identified a weakly polarized disk feature or candidate "c." As mentioned in the 1, these directly imaged IR detections are being debated (Thalmann et al. 2016; Follette et al. 2017; Hord et al. 2017; Sissa et al. 2018).
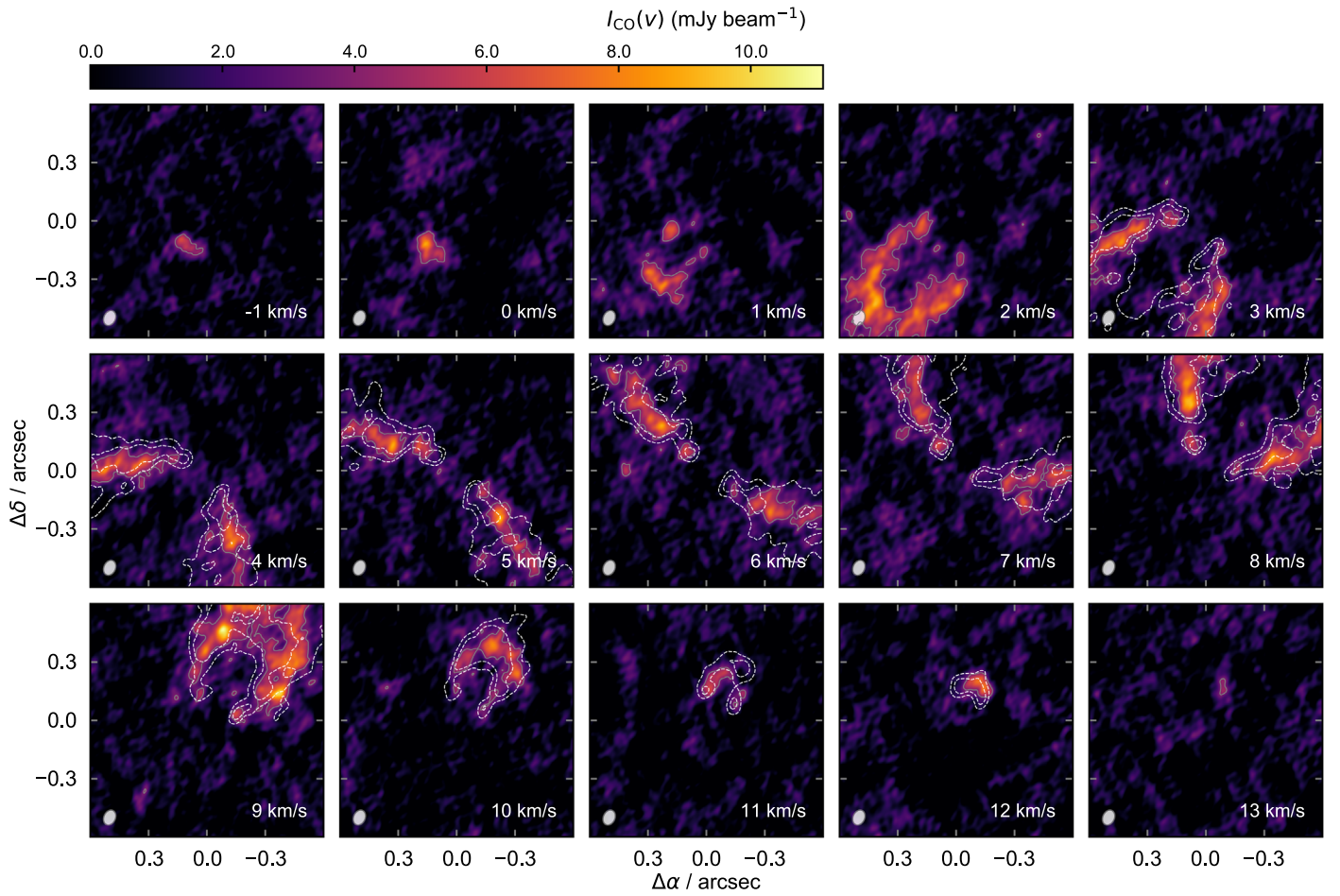
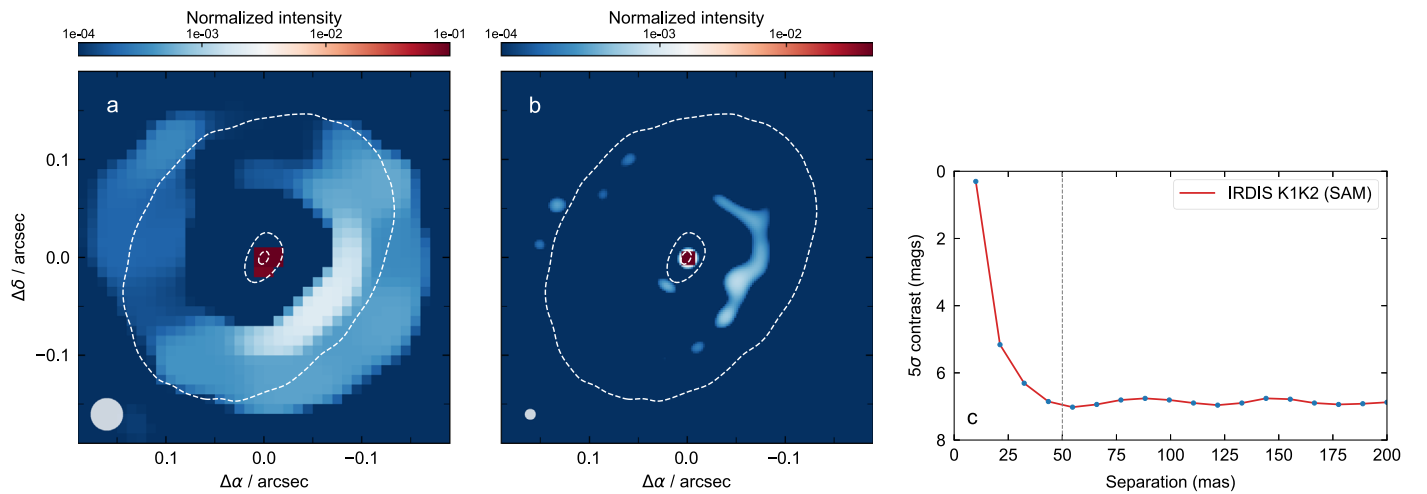**Figure 5.** Same as Figure 4, but for C$^{18}$O emission.



**Figure 6.** SPHERE SAM observations of HD 100546. The IRDIS (a) and IFS (b) images were produced with the MIRA package, applied to the closure phases and visibilities, with a hyperbolic regularization term. The images show extended scattered light and an empty gap free of stellar companions. The dashed contour shows the $9\sigma_{\rm MEM}$ level from the $I_{1.3\,\rm mm}$ continuum image. (c) IRDIS $5\sigma$ contrast curve for SAM observations in K1K2 band. A contrast of ∼7 mag is achieved between 50 and 200 mas.

On the other hand, spectroscopic monitoring of rovibrational CO emission shows variability that is consistent with a companion orbiting near the edge of the gas cavity (Brittain et al. 2014, 2019). Although this companion would orbit farther away from the star (∼0″.1) than the deviation in kinematics seen within the cavity (∼60 mas), it may well be connected to the origins of gap and the non-Keplerian low-$J$ $^{12}$CO emission.

The velocity dispersion map $\sigma_{\rm vel}$ shows arm-like structures on top of the continuum ring (Figure 1(d)). This is also expected if the gap is being carved by a giant planet, via the observable kinematics of meridional circulations (Dong et al. 2019). Within

the gap, the line broadens abruptly at $\sim$50 mas at the same location that the velocity field twists its PA. A comparison with hydrodynamic predictions is being developed and will be presented in a future publication.

### 3.3. Could the Gap Be Opened by a Stellar Object?

The SAM observations (Figure 6) reveal extended signal (probably scattered light) from the disk, and a protoplanetary gap of smaller radius than the one in the millimeter continuum (shown here in dashed contours). Rather, the scattered light signal seems to delineate a region within the gap that matches the radius at which the gaseous velocity field becomes highly perturbed. The IRDIS image recovers emission from every PA, while IFS only yields signal from the maximum forward scattering angle (toward the southwest). The gap is empty at the achieved contrast level.

At the separation of <50 mas, the contrast in magnitude is 6.9 (Figure 6(c)). To convert this $5\sigma$ contrast in upper limits on the mass of putative companions, we used the BT-Settl models by Allard et al. (2012), adapted for SPHERE filters. This limit corresponds to a mass of 33 $M_{\rm Jup}$ if we assume the youngest age of 4 Myr for the star, or 71 $M_{\rm Jup}$ for the eldest of 12 Myr. We can exclude the presence of stellar companions around HD 100546.

### 4. Summary and Conclusions

In this Letter we presented high-resolution 1.3 mm observations of HD 100546 with ALMA. The continuum reveals an optically thick and rather wide ring, extending from 15 to 45 au in radius. The unprecedented angular resolutions, in this source, revealed a network of ridges, hitherto unseen in any such ring.

The velocity field of this protoplanetary disk shows strong signatures of non-Keplerian flows, most remarkably in the form of strong wiggles in the channel maps, from $0\rlap{.}''2$ to $0\rlap{.}''3$ northeast from the star, and extending over almost 90° in azimuth. The spiral wakes of an accreting giant planet could affect the line-of-sight velocities in a way that resembles the observed wiggles.

The $^{12}$CO channel maps show that the wiggles trace the blueshifted emission associated with a Doppler flip in the deviation from axially symmetric kinematics (presented in Casassus & Pérez 2019). This sign reversal is expected from planet–disk interaction simulations. The redshifted Doppler flip emission is difficult to identify in the global kinematics by inspecting the channel maps alone. Thus, observationally and without recourse to hydrodynamic simulations, the location of the presumed perturber cannot easily be pinpointed by the wiggles but rather by the Doppler flip.

The qualitative absence of kinematic wiggles in the rarer isotopologues is consistent with them being weaker at lower disk heights, and suggests that most of the perturbed flow is associated with vertical motions in the disk surface. Our observations also show enhanced dispersion in velocity at the stellocentric radius of the Doppler flip, which could reflect meridional flows in the context of a planet–disk interaction (Teague et al. 2019).

It is remarkable that the kinematic signature coincides with bright continuum emission. This is counterintuitive as an accreting planet is expected to open a deep gap in the dust density field, which is why we did not attempt to produce a
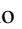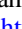
matching hydrodynamical simulation with a single giant (as in Pinte et al. 2018). Such a configuration may perhaps be reproduced with a closer-in giant (such as a that proposed by Brittain et al. 2019), which sustains the ring structure while a rapidly accreting giant planet is embedded within the ring.

*Facilities:* ALMA Observatory, VLT/SPHERE.

*Software:* GPUVMEM (Cárcamo et al. 2018), CASA (McMullin et al. 2007), MIRA (Thiébaut 2008).

### ORCID iDs

Sebastián Pérez https://orcid.org/0000-0003-2953-755X
Simon Casassus https://orcid.org/0000-0002-0433-9840
Antonio Hales https://orcid.org/0000-0001-5073-2849
Sebastián Marino https://orcid.org/0000-0002-5352-2924
Anthony Cheetham https://orcid.org/0000-0003-3943-4044
Alice Zurlo https://orcid.org/0000-0002-5903-8316
Lucas Cieza https://orcid.org/0000-0002-2828-1153
Ruobing Dong https://orcid.org/0000-0001-9290-7846
Felipe Alarcón https://orcid.org/0000-0002-2692-7862
Pablo Benítez-Llambay https://orcid.org/0000-0002-3728-3329
Ed Fomalont https://orcid.org/0000-0002-9036-2747
Henning Avenhaus https://orcid.org/0000-0002-1302-4613

### References

Allard, F., Homeier, D., & Freytag, B. 2012, RSPTA, 370, 2765
ALMA Partnership, Brogan, C. L., Pérez, L. M., et al. 2015, ApJL, 808, L3
Andrews, S. M., Huang, J., Pérez, L. M., et al. 2018, ApJL, 869, L41
Andrews, S. M., Wilner, D. J., Zhu, Z., et al. 2016, ApJL, 820, L40
Biller, B. A., Males, J., Rodigas, T., et al. 2014, ApJL, 792, L22
Brittain, S. D., Carr, J. S., Najita, J. R., Quanz, S. P., & Meyer, M. R. 2014, ApJ, 791, 136
Brittain, S. D., Najita, J. R., & Carr, J. S. 2019, ApJ, 883, 37
Cárcamo, M., Román, P. E., Casassus, S., Moral, V., & Rannou, F. R. 2018, A&C, 22, 16
Casassus, S., Marino, S., Pérez, S., et al. 2015, ApJ, 811, 92
Casassus, S., & Pérez, S. 2019, ApJL, 883, L41
Cheetham, A. C., Samland, M., Brems, S. S., et al. 2019, A&A, 622, A80
Christiaens, V., Cantalloube, F., Casassus, S., et al. 2019, ApJL, 877, L33
Christiaens, V., Casassus, S., Perez, S., van der Plas, G., & Ménard, F. 2014, ApJL, 785, L12
Close, L. M., Follette, K. B., Males, J. R., et al. 2014, ApJL, 781, L30
Currie, T., Cloutier, R., Brittain, S., et al. 2015, ApJL, 814, L27
Dipierro, G., Price, D., Laibe, G., et al. 2015, MNRAS, 453, L73

Dong, R., Li, S., Chiang, E., & Li, H. 2017, ApJ, 843, 127
Dong, R., Liu, S.-Y., & Fung, J. 2019, ApJ, 870, 72
Facchini, S., Pinilla, P., van Dishoeck, E. F., & de Juan Ovelar, M. 2018, A&A, 612, A104
Fedele, D., Carney, M., Hogerheijde, M. R., et al. 2017, A&A, 600, A72
Follette, K. B., Rameau, J., Dong, R., et al. 2017, AJ, 153, 264
Gaia Collaboration, Brown, A. G. A., Vallenari, A., et al. 2018, arXiv:1804.09365
Gressel, O., Nelson, R. P., Turner, N. J., & Ziegler, U. 2013, ApJ, 779, 59
Hord, B., Lyra, W., Flock, M., Turner, N. J., & Mac Low, M.-M. 2017, ApJ, 849, 164
Isella, A., Benisty, M., Teague, R., et al. 2019, ApJL, 879, L25
Keppler, M., Benisty, M., Müller, A., et al. 2018, A&A, 617, A44
Lubow, S. H., Seibert, M., & Artymowicz, P. 1999, ApJ, 526, 1001
McMullin, J. P., Waters, B., Schiebel, D., Young, W., & Golap, K. 2007, in ASP Conf. Ser. 376, Astronomical Data Analysis Software and Systems XVI, ed. R. A. Shaw, F. Hill, & D. J. Bell (San Francisco, CA: ASP), 127
Miki, S. 1982, PThPh, 67, 1053
Ober, F., Wolf, S., Uribe, A. L., & Klahr, H. H. 2015, A&A, 579, A105
Pavlov, A., Feldt, M., & Henning, T. 2008, in ASP Conf. Ser. 394, Astronomical Data Analysis Software and Systems XVII, ed. R. W. Argyle, P. S. Bunclark, & J. R. Lewis (San Francisco, CA: ASP), 581

Pérez, S., Casassus, S., Baruteau, C., et al. 2019a, AJ, 158, 15
Pérez, S., Casassus, S., & Benítez-Llambay, P. 2018, MNRAS, 480, L12
Perez, S., Dunhill, A., Casassus, S., et al. 2015, ApJL, 811, L5
Pérez, S., Marino, S., Casassus, S., et al. 2019b, MNRAS, 488, 1005
Pineda, J. E., Szulágyi, J., Quanz, S. P., et al. 2019, ApJ, 871, 48
Pinte, C., Price, D. J., Ménard, F., et al. 2018, ApJL, 860, L13
Pinte, C., van der Plas, G., Ménard, F., et al. 2019, NatAs, 3, 1109
Price, D. J., Cuello, N., Pinte, C., et al. 2018, MNRAS, 477, 1270
Quanz, S. P., Amara, A., Meyer, M. R., et al. 2013, ApJL, 766, L1
Ricci, L., Cazzoletti, P., Czekala, I., et al. 2017, AJ, 154, 24
Sissa, E., Gratton, R., Garufi, A., et al. 2018, A&A, 619, A160
Stolker, T., Sitko, M., Lazareff, B., et al. 2017, ApJ, 849, 143
Szulágyi, J., Morbidelli, A., Crida, A., & Masset, F. 2014, ApJ, 782, 65
Teague, R., Bae, J., & Bergin, E. A. 2019, Natur, 574, 378
Teague, R., Bae, J., Bergin, E. A., Birnstiel, T., & Foreman-Mackey, D. 2018, ApJL, 860, L12
Thalmann, C., Janson, M., Garufi, A., et al. 2016, ApJL, 828, L17
Thiébaut, E. 2008, Proc. SPIE, 7013, 70131I
van der Plas, G., Wright, C. M., Ménard, F., et al. 2017, A&A, 597, A32
Weber, P., Pérez, S., Benítez-Llambay, P., et al. 2019, ApJ, 884, 178
Wu, Y.-L., Close, L. M., Eisner, J. A., & Sheehan, P. D. 2017, AJ, 154, 234
Zhu, Z., Andrews, S. M., & Isella, A. 2018, MNRAS, 479, 1850